Determination of smoke plume and layer heights using scanning lidar data

Vladimir A. Kovalev,* Alexander Petkov, Cyle Wold, Shawn Urbanski, and Wei Min Hao

United States Forest Service, Rocky Mountain Research Station, Fire Sciences Laboratory, 5775 Highway 10 West, Missoula, Montana 59808, USA

*Corresponding author: vkovalev@fs.fed.us

Received 12 June 2009; revised 12 August 2009; accepted 20 August 2009; posted 20 August 2009 (Doc. ID 112716); published 21 September 2009

The methodology of using mobile scanning lidar data for investigation of smoke plume rise and high-resolution smoke dispersion is considered. The methodology is based on the lidar-signal transformation proposed recently [Appl. Opt. **48**, 2559 (2009)]. In this study, similar methodology is used to create the atmospheric heterogeneity height indicator (HHI), which shows all heights at which the smoke plume heterogeneity was detected by a scanning lidar. The methodology is simple and robust. Subtraction of the initial lidar signal offset from the measured lidar signal is not required. HHI examples derived from lidar scans obtained with the U.S. Forest Service, Fire Sciences Laboratory mobile lidar in areas polluted by wildfires are presented, and the basic details of the methodology are discussed. © 2009

OCIS codes: 280.3640, 290.1350, 290.2200.

1. Introduction

Recent decades have witnessed an increase in the frequency, duration, and severity of wildfires in the western United States. Fires are a major source of fine particulates ($PM_{2.5}$) and ozone (O_3), pollutants that are detrimental to human health and degrade visibility. Heightened concerns about the impact of poor air quality on public health and the more strenuous regulatory environment established by the Environmental Protection Agency elevate the need for air regulatory and land management agencies to address the contribution of fires to air pollution.

To comply with regulatory rules, land management agencies and air regulators need modeling tools to accurately predict the contribution of fire emissions to visibility impairment and $PM_{2.5}$ and O_3 pollution. Unfortunately, the ability of existing models to simulate smoke production and dispersion has not been thoroughly tested. The uncertainties and biases of these models and the limits of their applications are mostly unknown or poorly characterized, which is due mostly to the lack of adequate data for evaluation. The few smoke dispersion data sets available for model validation were from prescribed fires [1–3], which often differ significantly from wildfires in fuel conditions and meteorology.

To validate plume rise and high-resolution smoke dispersion models for a wide range of meteorological, fire behavior, fuel, and terrain conditions, smoke plume rise, dynamics, and transport in the near and far vicinities of wildfires should be investigated. This will allow for the rigorous evaluation of plume rise and high-resolution smoke dispersion models. More specifically, measurements of plume height and dispersion, made by a mobile lidar at different distances from wildfires combined with airborne *in situ* measurements will be performed and analyzed, and the results will be directly compared to the output of smoke plume rise models and high-resolution smoke dispersion forecasts. These comparisons can provide quantitative information with regard to the uncertainties, biases, and application limits of smoke dispersion and air quality forecasting systems, such as the National Oceanic and Atmospheric Administration Air Resources Laboratory hybrid single-particle Lagrangian integrated trajectory (HYPSLIT) model and the U.S. Forest Service Weather Research and

0003-6935/09/285287-08$15.00/0

Forecast Smoke Dispersion and Blue Sky Smoke Prediction systems.

Mobile ground-based remote-sensing instrumentation, such as a scanning lidar, is the most appropriate tool for ground-based monitoring of wildfire smoke-plume dynamics and heights at different distances from the wildfires. Lidar is the only instrument capable of obtaining highly detailed, three-dimensional range and height-resolved information for smoke distributions and optical properties over ranges as long as 10 km or more. Such instrumentation can operate from a position far outside the burning area with complete safety for the personnel involved. Lidar allows continuous monitoring of smoke-polluted atmospheres adjacent to severe wildfires and investigation of temporal and spatial variation of aerosol properties, plume heights and dynamics, and direction and rate of smoke plume movement in near real time. Lidar temporal data series can reveal strong downdrafts that transport smoke particulates downward, worsening air quality at ground level.

Most smoke plume optical and microphysical studies were made with a one-directional lidar, usually vertically pointed [4–6]. There is much less investigation of smoke plumes with a scanning lidar; for these studies, mostly azimuthally scanning lidar was used. The measurement methodology in these studies is generally based on the use of a conventional lidar equation solution adapted for the conditions of heterogeneous smoke-polluted atmospheres [7–10]. Vertically scanning lidar is utilized quite rarely, generally for specific tasks, such as determining the travel velocity of smoke plume formations from synchronous lidar and video observations [11].

Our current study focuses on the methodology of using lidar vertical scans of smoke plumes to extract information about the plume height and its spatial and temporal changes. Until now, no accepted methodology for processing such data exists. We achieve this objective by using a new technique that determines a special intercept function and transforms it into what we define here as the atmospheric heterogeneity height indicator (HHI). To determine smoke boundaries, we utilize a new way of applying the technique described in [12].

2. Method

A. Principle of the Smoke-Plume-Boundary Determination

To monitor smoke plume behavior, the regions with high levels of backscattering must be discriminated from regions of clear atmosphere, and the distance from the lidar to the smoke plume edges should be established. In principle, lidar can easily detect the boundary between different atmospheric layers. Subjective identification of heterogeneous areas, such as the atmospheric boundary layer or clouds, in lidar scans through visual inspection is often a trivial matter. However, the use of an automated method to determine these boundaries is a significant challenge. Generally, the heterogeneity boundaries in the atmosphere are not well defined, especially in smoke plumes, where the dispersion processes create a continuous transition zone between clear air and the dense part of a plume.

Different methodologies have been proposed to identify regions of intense backscatter with lidar. The most advanced techniques for determining boundary between clear air and the area with increased particulate loading were developed during numerous studies of the boundary layer [13–20]. It follows from these that the process of setting criteria for determining the boundaries of atmospheric heterogeneous layers is always highly subjective and different methods can yield different results [13]. Therefore, a variety of lidar data-processing methods have been tested and used to determine the atmospheric boundary layer. Initially, the height was found by establishing a threshold level of the backscatter signal [14,15]. A more popular technique for determination of the boundary layer height was based on the calculation of either the first-order or the second-order derivative of the square-range-corrected signal [13,16]. Other data-processing techniques focus on the behavior of the variance or covariance profiles of the lidar signal [17–20]. Optical conditions can vary greatly, no one technique can be considered universal. Currently the wavelet covariance transform technique is considered as most practical [19,20].

The basic issue with smoke measurement is the absence of a practical lidar measurement methodology to determine parameters of interest that are properly adapted to the specifics of the smoke-polluted atmosphere. Accumulated experience from investigation of the boundary layer is helpful. However, the structure and the temporal and spatial changes of smoke plumes in the vicinity of wildfires differ dramatically from the features typically present in the entrainment zone of undisturbed atmosphere. Temporal changes of the backscatter coefficient values in smoke plumes can be much larger than those in the boundary layer. Moreover, spatial gradients in the backscatter at the smoke plume edge, which must be determined to locate the smoke boundary, have an extremely wide range of values.

The basic principle of the proposed lidar data-processing scheme is the same as for any other method for determination of atmospheric heterogeneity—to identify ranges where increased gradients in the backscatter signal exist. However, unlike commonly used methods, we utilize an alternative variant that does not require initial separation of the background component in the recorded lidar signal. We omit all procedures associated with calculating the constant offset in the lidar signal, its subtraction, and calculating the corresponding square-range-corrected signals. To determine the smoke layer and plume heights and monitor their changes over time, we apply the same lidar signal transformation as used in [12]. Our analyses revealed that this transformation could also be adapted for our current task of

determining the heights and boundaries of areas with increased aerosol loading.

The original signal $P_\Sigma(r)$ recorded by the lidar from range r is the sum of a backscatter signal $P(r)$ and an offset B, created by a daytime background illumination and electrical or digital offset. For the ranges of the complete overlap zone, the signal can be written as

$$P_\Sigma(r) = \frac{1}{r^2} C[\beta_{\pi,m}(r) + \beta(r_{\pi,p})] \times [T_m(0,r)]^2 [T_p(0,r)]^2 + B, \quad (1)$$

where C is a lidar constant, which also includes the transmitted light pulse energy; $\beta_{\pi,m}(r)$ and $\beta_{\pi,p}(r)$ are the molecular and particulate backscatter coefficients; $[T_m(0,r)]^2$ and $[T_p(0,r)]^2$ are the molecular and particulate two-way transmission from the lidar to range r, respectively. Following the procedures described in [12], the signal is transformed into the function $Y(r) = P_\Sigma(r)x(r)$, where $x(r)$ is defined in a general form as

$$x(r) = \frac{r^2}{\beta_{\pi,m}(r)[T_m(0,r)]^2}. \quad (2)$$

The function $Y(r)$ can then be written in the form

$$Y(r) = W_p(r) + Bx(r), \quad (3)$$

where $W_p(r) = C[1 + R_\beta(r)][T_p(0,r)]^2$ and $R_\beta(r) = \beta_{\pi,p}(r)/\beta_{\pi,m}(r)$. After rewriting these expressions as functions of variable x, the derivative dY/dx can be written in the form

$$dY/dx = d/dx[W_p(x) + Bx], \quad (4)$$

and the corresponding intercept, $Y_0(x)$, with the vertical axis as

$$Y_0(x) = Y(x) - \frac{dY}{dx}x. \quad (5)$$

Calculation of the running numerical derivative dY/dx and the corresponding $Y_0(x)$ allows one to determine the ranges where the gradient of $R_\beta(r)$ and, accordingly, the function $W_p(r)$ change in space. Note that, for the task considered here, estimation of offset B is not required. Moreover, knowledge of the molecular profile is not mandatory if the lidar operates at wavelengths at which the molecular extinction is negligible; then the variable $x(r)$ can be reduced to $x(r) = r^2$.

The principle of determining the location of the increased backscatter gradient using numerical differentiation of the function $Y(x)$ is clarified in Figs. 1 and 2. In Fig. 1, the dotted curve shows the model profile of the particulate extinction coefficient, $\kappa_p(x)$, used for the calculation. The shape of the profile is modeled on the basis of typical extinction-coefficient

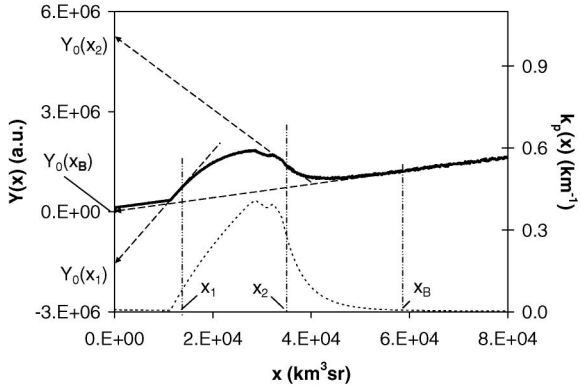

Fig. 1. Model profile of the particulate extinction coefficient (dotted curve) and the corresponding function of $Y(x)$ (solid curve).

profiles that we obtained from measurements in smoky atmospheres; the boundaries of the model smoke plume are not well defined, as is often the case in real situations. The increased particulate loading caused by a smoke plume was presumably located between ~3400 and ~6000 m, which corresponds to the values of $x = 12000\,\mathrm{km^3\,sr}$ and $x = 53600\,\mathrm{km^3\,sr}$. The dependence of $Y(x)$ versus x calculated from a corresponding noise-corrupted synthetic lidar signal is shown as the solid curve. When the sliding derivative with a range resolution of $\Delta r = \text{const.}$ is determined over the range where $x \geq x_B$, the intersect point, $Y_0(x_B)$, remains close to the value of 4.8×10^4 a.u. In the regions of the smoke plume where the gradient of $R_\beta(r)$ changes, the intersect of the linear fit, $Y_0(x)$, varies from -1.5×10^6 to 5.4×10^6 a.u. [points $Y_0(x_1)$ and $Y_0(x_2)$, respectively].

The intercept function, $Y_0(x)$, is rewritten as a function of range $Y_0(r)$, and its absolute value $|Y_0(r)|$ is then used to determine ranges with an increased gradient of aerosol loading. In Fig. 2, the function of $|Y_0(r)|$ (solid curve) for the same model profile of the particulate extinction coefficient $\kappa_p(r)$ (dotted curve) is shown. In smoke plume areas with the increased $\kappa_p(r)$, the function $|Y_0(r)|$ is much larger than that observed in adjacent clear air. Therefore, the ranges of the near-end sharp increase and the far-end sharp decrease of $|Y_0(r)|$ can be considered as boundaries of

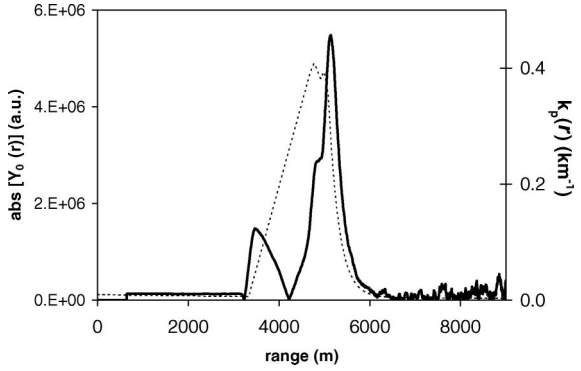

Fig. 2. Model profile of the particulate extinction coefficient $\kappa_p(r)$ (dotted curve) and the corresponding function of $|Y_0(r)|$ (solid curve).

the increased backscatter gradient. To decrease the difference in the maximum values of $|Y_0(r)|$ at the near and far ends, a normalization of the $|Y_0(r)|$ is made as described below.

B. Determination of Smoke-Plume Boundaries and Heights Using the Heterogeneity Height Indicator

The single direction lidar cannot provide the required information when investigating smoke plume dynamics. The only exception would be the case of extended horizontal smoke layering in a stable atmospheric inversion. In most cases, multiangle measurement is the only practical option for utilization of lidar in the vicinity of the wildland fire.

In the case of multiangle measurements, Eq. (3) should be rewritten in the form

$$Y(r,\varphi) = W_p(r,\varphi) + B_\varphi\, x(r,\varphi), \tag{6}$$

where φ is the slope angle under which lidar searching takes place; $W_p(r,\varphi) = C_\varphi[1 + R_\beta(r,\varphi)][T_{p,\varphi}(0,r)]^2$ and $R_\beta(r,\varphi) = B_{\pi,p}(r,\varphi)/B_{\pi,m}(r,\varphi)$. For simplicity, it is assumed here that $B_\varphi = \text{const}$. However, for the current task, this condition is not important. After transforming the expression in Eq. (6) into functions of variable x, the intercept $Y_0(x,\varphi)$ can be determined as

$$Y_0(x,\varphi) = Y_\varphi - \frac{dY_\varphi}{dx_\varphi} x_\varphi, \tag{7}$$

where dY_φ/dx_φ is determined locally as

$$\frac{dY_\varphi}{dx_\varphi} = \frac{d}{dx}[W_p(x_\varphi,\varphi) + B_\varphi x_\varphi]. \tag{8}$$

Note that the local numerical sliding derivative is determined over ranges with constant resolution Δr rather than with constant Δx. Equation (7) yields the intercept function, $Y_0(x,\varphi)$, for each slope direction φ. To better discriminate multiple layering over extended height ranges, we normalize the original function $Y_0(x,\varphi)$. The normalized function for each slope direction, $Y_0^*(x,\varphi)$, is defined as

$$Y_0^*(x,\varphi) = \frac{Y_0(x,\varphi)}{x(\varphi) + \Delta_\varphi}, \tag{9}$$

where Δ_φ is a user-defined positive nonzero constant that can be chosen within the range $(0.02–0.05)x_{\max}(\varphi)$, where $x_{\max}(\varphi)$ is the maximum value of $x(\varphi)$ over the selected height interval from $h_{\min}$ to $h_{\max}$. The goal of adding the component Δ_φ to the denominator in Eq. (9) is to avoid infinite increase of $Y_0^*(x,\varphi)$ when $x(\varphi) \to 0$, and, accordingly, too high values of $Y_0^*(x,\varphi)$ close to $r_{\min}$. Note that the component Δ_φ does not influence $Y_0^*(x,\varphi)$ at the distances of interest, where $x(\varphi) \gg \Delta_\varphi$; therefore, the selection of concrete value Δ_φ is not critical.

The normalized intercept function $Y_0^*(x,\varphi)$ is transformed to a function of height with the form $Y_0^*(h,\varphi)$. The regions in which its absolute value $|Y_0^*(h,\varphi)|$ increases are the regions with increased backscatter gradient and can be examined to identify smoke plume boundaries. To determine these boundaries, we implemented what we call the HHI.

In Figs. 3 and 4, the principle of calculating the HHI profile from data of an artificial scanning lidar in an imaginary atmosphere is clarified. In the model atmosphere, shown in Fig. 3, a spatially restricted aerosol cloud C within the height range from h_1 to h_2 exists at some distance from the lidar located at point A. At higher altitudes, a horizontally stratified smoke plume layer L is located between heights h_3 and h_4. The scanning lidar measures backscatter signals under 17 slope directions. From these signals, the height-dependent normalized intercepts $|Y_0^*(h,\varphi)|$ are found and the areas with increased backscatter gradient are defined. When measuring signals from the smallest angles, along slopes 1 and 2, the laser beam propagates in the clear atmosphere, outside cloud C. Therefore, increased backscatter gradients are not observed in these signals. The smoke cloud C is the source of increased backscatter signals when the lidar scans at higher elevations, along slopes 3–6. In these signals, backscatter gradients increase at the corresponding heights from h_1 to h_2. Along slope 7, no cloud is detected. Presumably, horizontal layering L at higher altitudes h_3–h_4 is still not detected because of the restricted lidar measurement range. This layering is revealed when searching occurs along slope directions from 8 to 17. Note that, if cloud C is more or less homogeneous, the increased gradients will exist mainly on the edges of the cloud. In real conditions, however, a smoke cloud is rarely homogeneous, so the increased backscatter gradients would mostly be revealed at every step Δh within the height interval (h_1, h_2).

The set of profiles $|Y_0^*(h,\varphi)|$ calculated with some height resolution Δh allows one to plot the HHI profile. The HHI profile shows the heights at which

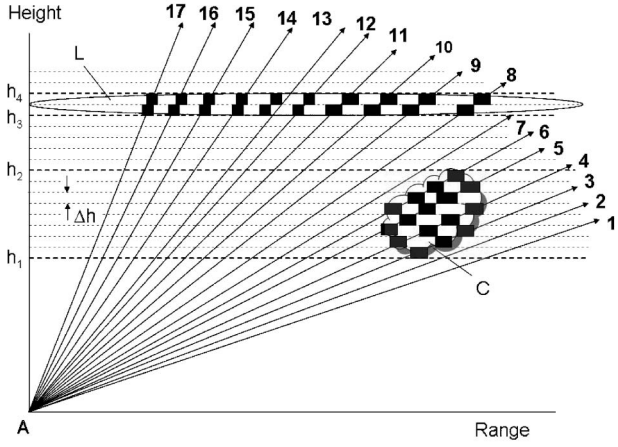

Fig. 3. Principle of determining locations with increased backscatter gradient in the lidar scan. Lidar is located at point A. The filled rectangles show areas with increased backscatter.

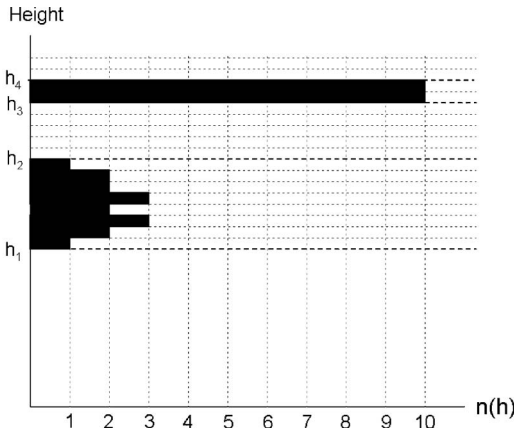

Fig. 4. HHI plot showing heights and the number of heterogeneity events $n(h)$ along which the increased smoke-plume gradients were revealed.

increased smoke-plume backscatter gradients occur and under how many slope directions these were observed. In other words, the HHI plot shows a number of heterogeneity events, $n(h)$, fixed at different heights within the area searched by the lidar (Fig. 4). This plot shows not only the smoke plume altitude ranges but also allows us to distinguish the local smoke plume C from the extended smoke layering L. One can see from Fig. 4 that the increased backscatter gradient in the layer located over the height interval from h_3 to h_4 is detected along ten elevation angles (from 8 to 17), that is, the number of heterogeneity events at these altitudes is $n(h) = 10$. For cloud C, within the height interval from h_1 to h_2, the increased backscatter gradient is visible only over two or three slope directions.

3. Essentials of the Multiangle Data Processing Methodology

When measuring wildfire smoke layering and plumes with lidar, we can encounter different situations. In particular we identify four basic situations that can be commonly met during measurements in the vicinity of fires:

(a) highly dispersed smoke haze, generally, downwind from large fires,
(b) well-defined smoke horizontal layering above the boundary layer created by atmospheric inversion,
(c) dense smoke plume centered over a single intense fire spot, and
(d) spotted local fire plumes scattered within an extended wildfire area.

For (c) and (d), the lidar signals from the smoke plumes are obtained only in restricted azimuthal and zenith sectors. For (a) and (b), azimuthal and zenith limits are restricted only by characteristics of the landscape.

To clarify how smoke plume heights and layer outlines are found, let us consider some measurement results obtained with the U.S. Forest Service, Fire Sciences Laboratory lidar when scanning smoke plumes created by wildfires. Figure 5(a) shows the conventional range height indicator (RHI) plot for the range-corrected signals, retrieved from a lidar vertical scan recorded at 1064 nm wavelength during the Montana I-90 Fire, at 11:37 a.m. on 9 August 2005. The lidar scanned vertically over thirty-seven slope directions, from $\varphi_{\min} = 7.5°$ to $\varphi_{\max} = 79.5°$, with angular separation $\Delta\varphi = 2°$. One can see multiple horizontally stratified layers between the heights of ~1000 and ~2500 m. This situation is typical for case (b).

It is interesting to compare the conventional RHI plot with a similar plot built by using a colored scale for the absolute normalized intercept values, $|Y_0^*(h,\varphi)|$, instead of the attenuated backscatter. In Fig. 5(b), such a plot is shown calculated for the same data as those used for Fig. 5(a). The plot, in which the colored scale shows the absolute normalized intercept in arbitrary units, can be defined as the heterogeneity RHI (HRHI). When the dispersed smoke

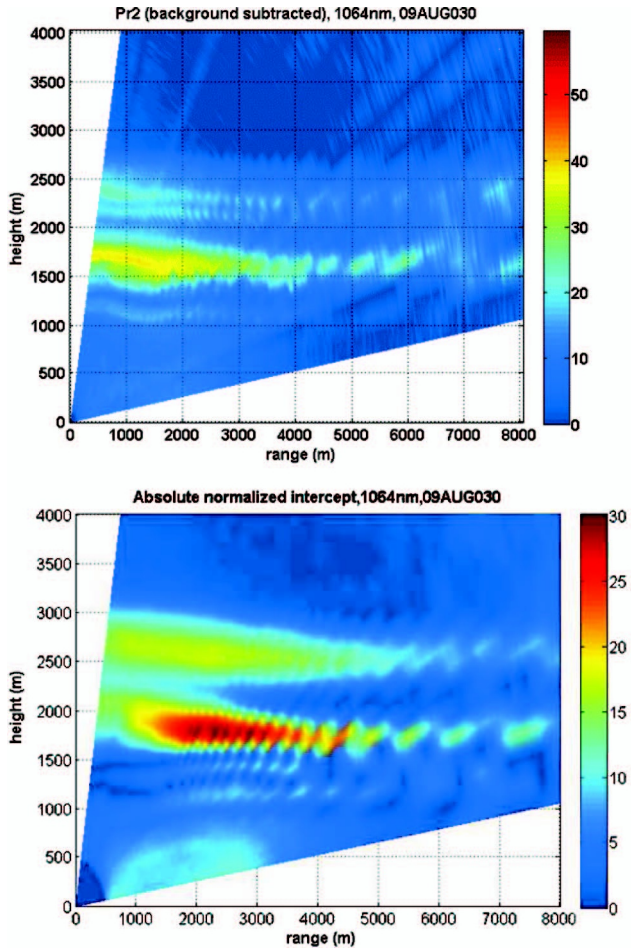

Fig. 5. (a) Conventional RHI scan from data recorded at 1064 nm wavelength during the Montana I-90 Fire at 11:37 a.m. on 9 August 2005. The colored scale shows the attenuated backscatter intensity in arbitrary units. (b) HRHI scan for the same data. The colored scale shows the absolute normalized intercept in arbitrary units.

plumes are the subject of interest, such a plot can be more informative than the conventional RHI plot.

Description of the retrieval process for the HHI plot follows. For each slope direction φ, we calculate the function $Y(r,\varphi)$ and transform it into the function of x. Then the sliding numerical derivative dY_φ/dx_φ, with some range resolution Δr is found, and the corresponding functions $Y_0(x,\varphi)$ and $Y_0^*(x,\varphi)$ for each elevation angle are determined. The normalized intercept $Y_0^*(x,\varphi)$ is rewritten as a function of height $Y_0^*(h,\varphi)$, and its absolute values, expressed as $|Y_0^*(h,\varphi)|$, are calculated.

Before boundaries of the areas with increased gradient of $R_\beta(r,\varphi)$ are established, the maximum of all functions $|Y_0^*(h,\varphi)|$ over the established height interval from $h_{\min}$ to $h_{\max}$ is found:

$$Y_{\max}^* = \max[\max|Y_0^*(h,\varphi_1)|, \max|Y_0^*(h,\varphi_2)|, \ldots \max|Y_0^*(h,\varphi_{N-1})|, \max|Y_0^*(h,\varphi_N)|], \quad (10)$$

where φ_N is the maximum slope angle, and N is the total number of directions in the analyzed scan; in our case, $N = 37$. The boundaries of areas with increased gradient of $R_\beta(r,\varphi)$ are established as the locations where the functions $|Y_0^*(h,\varphi)|$ reach some established (user defined) level relative to the above value of $Y_{\max}^*$. In other words, the smoke location is determined as the ranges or heights at which $|Y_0^*(h,\varphi)| \geq \chi Y_{\max}^*$; here $0 < \chi < 1$.

In Fig. 6, the HHI plot for the above case under consideration is shown (filled rectangles) calculated with $\chi = 0.3$. The HHI shows that the layer with increased gradients extends from the height of $h_{\mathrm{sm,max}} = 3100$ m to the minimal searched height, $h_{\mathrm{sm,min}} = 300$ m, with an increased heterogeneous layer over the upper heights of 1500–3100 m. Here height $h_{\mathrm{sm,min}}$ is determined as the maximal height below which all $n(h) = 0$ and $h_{\mathrm{sm,max}}$ as the minimal height above which all $n(h) = 0$. In the presence of scattered noise data points in the HHI, some minimal nonzero level can be established to determine $h_{\mathrm{sm,min}}$ and $h_{\mathrm{sm,max}}$. The dashed curve in Fig. 6 shows the shape of the mean function $|Y_0^*(h)|_{\mathrm{mean}}$ for all slope directions $N = 37$ in arbitrary units; for convenience, it is normalized here to the $n(h)$ scale as follows:

$$|Y_0^*(h)|_{\mathrm{norm}} = \frac{|Y_0^*(h)|_{\mathrm{mean}} n(h)_{\max}}{|Y_0^*(h)|_{\mathrm{mean,max}}}, \quad (11)$$

where $n(h)_{\max}$ is the maximum value of the heterogeneity events over the heights from $h_{\min}$ to $h_{\max}$. Currently the mean function is used only for visual inspection and comparison with the shape of the retrieved HHI plot; however, potentially it can be used as an additional constraint when determining the minimum and maximum smoke plume heights.

The obvious question emerges: What level relative to $Y_{\max}^*$ should be used to determine the smoke boundary in the condition of dispersed smoke, where no sharp transition from the smoke plume to clear air takes place? Obviously, there is no general answer to this question, and the researcher should decide this question based on analysis of the retrieved data. The selection of low χ ($\chi < 0.2$) will increase sensitivity of the measured results to small-scale heterogeneity and signal noise fluctuations. As a result, it might be difficult to distinguish the information of interest from noise. The selection of high χ ($\chi > 0.5$) might be sensible when one needs to determine the location of the most intense heterogeneity area. However, it can result in overlooking optically thin smoke plumes, especially with clouds in the background. Obviously, parameter χ should be chosen depending on the concrete task of the experiment.

To make an optimum selection of χ, it might be useful to analyze how the retrieved smoke plume heights depend on the value of the selected χ. Such a dependence of the heights of interest, $h_{\mathrm{sm,min}}$ and $h_{\mathrm{sm,max}}$ versus χ for the same case as in Fig. 5 is shown in Fig. 7. One can see that, with χ up to 0.35, the smoke plume is observed starting somewhere below the lidar minimal measurement height of $h_{\min} = 300$ m. The values of χ over the wide range from 0.4 to 0.9 yield the height $h_{\mathrm{sm,min}}$, which increases by less than 10% from 1576 to 1712 m. This observation means that, at these heights, the smoke

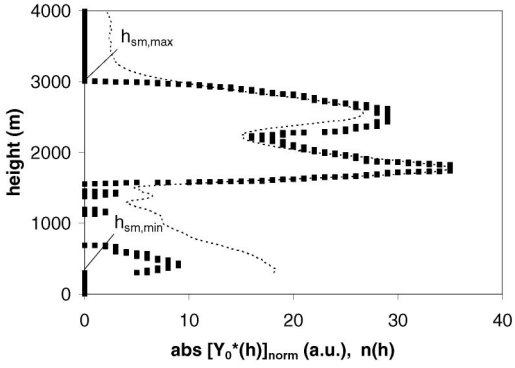

Fig. 6. HHI for the same case as in Fig. 5 calculated with $\chi = 0.3$ (filled rectangles) and the corresponding $|Y_0^*(h)|_{norm}$ (dashed curve).

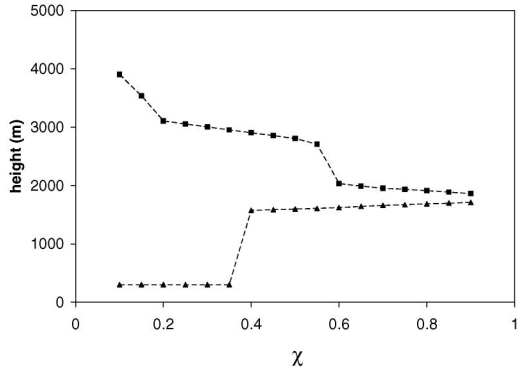

Fig. 7. Dependence of the heights $h_{\mathrm{sm,min}}$ and $h_{\mathrm{sm,max}}$ on the selected χ for the same case as in Fig. 5.

Fig. 8. Smoke plume observed during the Tripod Complex Fire (Washington) on 21 August 2006.

plume boundary is well defined. Similarly, with χ from 0.2 to 0.5, relatively well-defined boundaries of maximum heights $h_{\mathrm{sm,max}}$ are observed over the heights, approximately 2800–3100 m. The most intense layer with $|Y_0^*(h,\varphi)|$ close to $Y_{\max}^*$, found with $\chi = 0.6$–0.9, is located in the height interval from ~1700 to ~1900 m.

Finally, let us consider a case typical for situation (c). We examined such a case (shown in Fig. 8) during the Tripod Complex Fire in Washington state on 21 August 2006. The measurement site was located at 1496 m above sea level.

A typical HHI plot for this case, obtained with $\chi = 0.3$, is shown in Fig. 9. The maximal height of the plume in this case reached 7794 m above ground level at the lidar measurement site. The mountain terrain of the site did not allow scanning under small elevation angles. The minimal slope angle used was 28°, and the recorded minimal height $h_{\mathrm{sm,min}}$ was 4548 m. The dependence of the minimum and maximum height on χ for this case is shown in Fig. 10. Within the range of χ from 0.15 to 0.4, the values of $h_{\mathrm{sm,min}}$ and $h_{\mathrm{sm,max}}$ fluctuate less than 1%, and the largest values of $|Y_0^*(h,\varphi)|$ were found with $\chi = 0.8$–0.9 at the height interval of ~5100–5800 m.

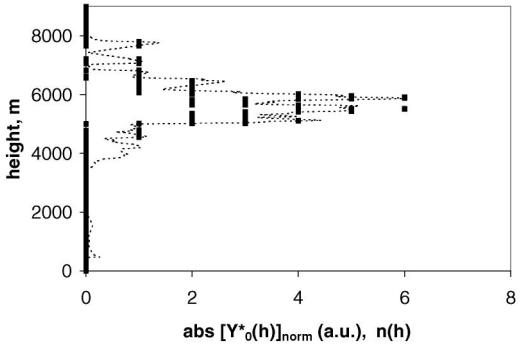

Fig. 9. HHI plot (filled rectangles) retrieved from the lidar scan recorded during the Tripod Complex Fire (Washington) on 21 August 2006. The dashed curve represents the corresponding normalized function $|Y_0^*(h)|_{norm}$.

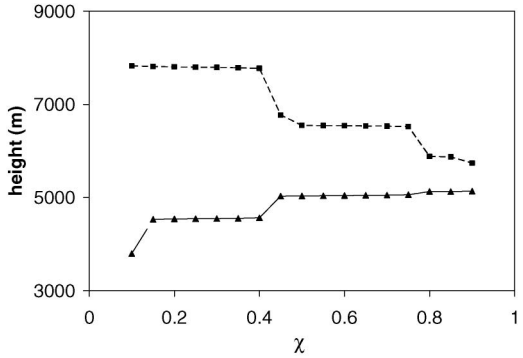

Fig. 10. Dependence of heights $h_{\mathrm{sm,min}}$ and $h_{\mathrm{sm,max}}$ on the selected χ for the same case as in Fig. 9.

4. Summary

The heterogeneity height indicator (HHI) allows one to determine the heights of smoke plumes and layers and their temporal change using data of the whole vertical scan, that is, to use the information obtained for the whole area searched by a scanning lidar. The distinctive feature of the HHI plot is that determination of the smoke boundaries is made by specifying the number of the heterogeneity events, that is, the number of the cases when the increased gradient is revealed at heights of interest. The HHI plot allows easy discrimination between a vertically developing smoke plume and a horizontally stratified smoke layer created by a morning inversion. It makes it possible to determine smoke plume vertical boundaries and their temporal changes using automated data processing. Analysis of an extended time series of HHI plots in areas close to large wildfires can reveal layers developing in the evening, their behavior overnight, and their evolution and breakup in the morning.

The proposed measurement technology for determination of smoke-plume boundaries and their spatial and temporal changes has three basic features. First, it can be utilized for all types of smoke formation regardless of smoke-plume parameters such as smoke heterogeneity, the dispersion level, the smoke plume density, the concentration levels, the spatial location and spread of smoke-polluted areas. Otherwise, no automatic data processing would be feasible. Second, all the available smoke plume information that exists in the vertical scan is used. Third, simple and physically sensible criteria are proposed that allow the determination of heights at which intense smoke plumes exist.

Unlike commonly used methods for determination of zones of increased backscatter signal gradient, the proposed methodology does not require preliminary estimation of the constant offset in the total signal and its subtraction. This feature will significantly

simplify the procedure for identification of the boundaries of smoke plumes of interest when processing our data in real time. Using this term, we imply that the measurement data can be processed by the time the next data set (scan) needs to be processed. It is easily achieved if the interval between consequent vertical scans is not less than ~10–15 min, which in most cases is reasonable for our tasks.

References

1. L. F. Radke, J. H. Lyons, P. V. Hobbs, D. A. Hegg, D. V. Sandberg, and D. E. Ward, "Airborne monitoring and smoke characterization of prescribed fires on forest lands in Western Washington and Oregon," Final General Technical Report PNW-GTR-251 (USDA Forest Service, 1990).
2. P. V. Hobbs, J. S. Reid, J. A. Herring, J. D. Nance, R. E. Weiss, J. L. Ross, D. A. Hegg, R. D. Ottmar, and C. Liousse, "Particle and trace-gas measurements in the smoke from prescribed burns of forest products in the Pacific Northwest," in *Biomass Burning and Global Change* (MIT Press, 1996), pp. 697–715.
3. P. V. Hobbs, P. Sinha, R. J. Yokelson, T. J. Christian, D. R. Blake, S. Gao, T. W. Kirchstetter, T. Novakov, and P. Pilewskie, "Evolution of gases and particles from a savanna fire in South Africa," J. Geophys. Res. **108**, doi:10.1029/2002JD002352 8485 (2003).
4. Y. J. Kaufman, J. M. Haywood, P. V. Hobbs, W. Hart, R. Kleidman, and B. Schmid, "Remote sensing of vertical distributions of smoke aerosol off the coast of Africa," Geophys. Res. Lett. **30** No. (16), doi: 10.1029/2003GL017068 1831 (2003).
5. D. Müller, I. Mattis, U. Wandinger, A. Ansmann, D. Althausen, and A. Stohl, "Raman lidar observation of aged Siberian and Canadian forest fire smoke in the free troposphere over Germany in 2003: Microphysical particle characterization," J. Geophys. Res. **110**, doi: 10.1029/2004JD005756, D17201 (2005).
6. G. R. McMeeking, S. M. Kreidenweis, C. M. Carrico, J. L. Colent, D. E. Day, and W. C. Malm, "Observations of smoke-influenced aerosol during the Yosemite Aerosol Characterization Study: 2. Aerosol scattering and absorption properties," J. Geophys. Res. **110**, doi: 10.1029/2004JD005624, D18209 (2005).
7. W. L. Eberhard, G. T. McNice, and S. W. Troxel, "Lidar sensing of plume dispersion: analysis methods and product quality for light-scattering tracer particles," J. Atmos. Ocean. Technol. **4** No. (4), 674–689 (1987).
8. W. L. Eberhard and W. R. Moninger, "Plume dispersion in the convective boundary layer. Part 1: CONDORS field experiment and example measurements," J. Appl. Meteorol. **27** No. (5), 599–616 (1988).
9. R. M. Banta, L. D. Oliver, E. T. Holloway, R. A. Kropfli, B. W. Bartram, R. E. Cupp, and M. J. Post, "Smoke-column observations from two forest fires using Doppler lidar and Doppler radar," J. Appl. Meteorol. **31** No. (11), 1328–1349 (1992).
10. A. Lavrov, A. B. Utkin, R. Vilar, and A. Fernandes, "Application of lidar in ultraviolet, visible, and infrared ranges for early forest fire detection," Appl. Phys. B **76**, doi:10.1007/s00340-002-1053-y, 87–95 (2003).
11. Yu. S. Balin, A. D. Ershov, P. A. Konyaev, and D. S. Lomakin, "Monitoring of the aerosol formations travel velocity in the atmosphere by use of video and lidar data," J. Atmos. Ocean. Opt. **17** No. (12), 885–890 (2004).
12. V. A. Kovalev, C. Wold, A. Petkov, and Wei Min Hao, "Alternative method for determining the constant offset in lidar signal," Appl. Opt. **48**, 2559–2584 (2009).
13. L. Menut, C. Flamant, J. Pelon, and P. H. Flamant, "Urban boundary-layer height determination from lidar measurements over the Paris area," Appl. Opt. **38**, 945–954 (1999).
14. S. H. Melfi, J. D. Spinhire, S. H. Chou, and S. P. Palm, "Lidar observations of vertically organized convection in the planetary boundary layer over the ocean," J. Clim. Appl. Meteorol. **24**, 806–821 (1985).
15. R. Boers and S. H. Melfi, "Cold-air outbreak during MASEX: lidar observations and boundary layer model test," Boundary-Layer Meteorol. **39**, 41–51 (1987).
16. C. Flamant, J. Pelon, P. H. Flamant, and P. Durant, "Lidar determination of the entrainment zone thickness and the top of the unstable marine atmospheric boundary layer," Boundary-Layer Meteorol. **83**, 247–284 (1997).
17. W. P. Hooper and E. W. Eloranta, "Lidar measurements of wind in the planetary boundary layer: the method, accuracy, and results from joint measurements with radiosonde and kytoon," J. Clim. Appl. Meteorol. **25**, 990–1001 (1986).
18. A. Piironen and E. W. Eloranta, "Convective boundary layer mean depths, cloud base altitudes, cloud top altitudes, cloud coverages, and cloud shadows obtained from volume imaging lidar data," J. Geophys. Res. **100**, 25569–25576 (1995).
19. I. M. Brooks, "Finding boundary layer top: Application of a wavelet covariance transform to lidar backscatter profiles," J. Atmos. Ocean. Technol. **20**, 1092–1105 (2003).
20. H. Baars, A. Ansmann, R. Engelmann, and D. Althausen, "Continuous monitoring of the boundary-layer top with lidar," Atmos. Chem. Phys. **8**, 7281–7296 (2008).